

Collision Cascade-Driven Evolution of Vacancy Defects in Ni-Based Concentrated Solid-Solution Alloys

A. Aligayev,^{1,2} M. Landeiro Dos Reis,³ A. Chartier,⁴ Q. Huang,² S. Papanikolaou,¹ and F. J. Domínguez-Gutiérrez*¹

¹*NOMATEN Centre of Excellence, National Center for Nuclear Research, 05-400 Swierk/Otwock, Poland*

²*Science Island Branch of Graduate School, University of Science and Technology of China, Hefei, 230026, China*

³*LaSIE UMR CNRS 7356, La Rochelle Université,*

Av. Michel Crépeau, 17042, La Rochelle Cedex 1, France

⁴*Université Paris-Saclay, CEA, Service de recherche en Corrosion et Comportement des Matériaux, 91191 Gif Sur Yvette, France*

Concentrated solid-solution alloys (CSAs) in single-phase form have recently garnered considerable attention owing to their potential for exceptional irradiation resistance. This computational study delves into the intricate interplay of alloying elements on the generation, recombination, and evolution of irradiation-induced defects. Molecular dynamics simulations were conducted for collision cascades at room temperature, spanning a range of primary knock-on atom energies from 1 to 10 keV. The investigation encompasses a series of model crystals, progressing from pure Ni to binary CSAs such as NiFe₂₀, NiFe, NiCr₂₀, and culminating in the more intricate NiFeCr₂₀ CSA. We observe that materials rich in chromium actively facilitate dislocation emissions and induce the nucleation of stacking fault tetrahedra in the proximity of nanovoids, owing to Shockley partial interactions. This result is validated by molecular static simulations, which calculate the surface, vacancy, and defect formation energies. Among various shapes considered, the spherical void proves to be the most stable, followed by the truncated octahedron and octahedron shapes. On the other hand, the tetrahedron cubic shape is identified as the most unstable, and stacking fault tetrahedra exhibit the highest formation energy. Notably, among the materials studied, NiCr₂₀ and NiFeCr₂₀ CSAs stood out as the sole alloys capable of manifesting this mechanism, mainly observed at high impact energies.

I. INTRODUCTION

Nickel and nickel-based concentrated solid solution alloys (CSAs) have been extensively investigated for their potential applications in harsh environments subjected to high irradiation doses [1–6] and could potentially serve as promising candidates for structural materials in nuclear applications, particularly in contexts where ensuring high radiation tolerance is a paramount consideration [7–9]. Recent successes in the fabrication of CSAs have paved the way for a new research direction aiming to substantially enhance alloy performance [1, 10–12]. While historical alloy development focused on traditional alloys with unique microstructural heterogeneity to mitigate displacement damage [13–16], CSAs represent a shift, containing two to five or more elements at high concentrations, sometimes in equal or near-equal amounts. The random arrangement of multiple elemental species on a crystalline lattice results in atomic-level elemental alternation, creating disordered local chemical environments [16–18]. This intrinsic property leads to unique site-to-site lattice distortions, creating complex energy landscapes that affect defect migration [5, 19, 20].

Considering the challenging service conditions of next-generation nuclear power reactors, which involve intense

radiation flux, higher operating temperatures, and high stress [21, 22], CSAs emerge as promising candidate materials for nuclear power applications [12, 20]. To be viable, these alloys must complement their superior mechanical properties with high radiation resistance [2, 6, 9, 10]. In reactor environments, irradiation-induced point defect formation, migration, and evolution are primary factors influencing microstructural changes that impact the performance of structural materials. Thus, controlling defect formation and migration in structural materials becomes crucial for designing materials with high radiation tolerance. The phenomenon of irradiation hardening is governed by the interactions between moving dislocations and irradiation induced defects occurring at the atomic scale [14, 23]. For instance, at doses around 0.01 dpa, the observation of softening becomes apparent in constant strain rate traction tests for materials relevant to nuclear applications [24]. Upon the initiation of plastic deformation, it is observed that the applied stress initially decreases and subsequently stabilizes. This phenomenon is associated with the formation and propagation of shear bands, characterized by the absence of any irradiation defect post-deformation [14, 15]. The emergence of these bands strongly suggests that, during their gliding, dislocations effectively eliminate irradiation defects [10, 20], which constitutes the primary focus of this work.

The kinetics and interaction of defects play a crucial role in controlling microstructural evolution, significantly impacting material properties over time [25–27]. We thus

* Corresponding author

F.J.D.G., e-mail: javier.dominguez@ncbj.gov.pl

investigate the influence of pre-existing defects on irradiation cascades, specifically examining common material defects such as vacancy clusters and stacking fault tetrahedra in elemental face-centered cubic (fcc) Ni, the two binary NiFe₂₀ and NiCr₂₀, and ternary NiFeCr₂₀ CSAs. We scrutinize several vacancy cluster shapes, from spherical to octahedron shape (in accordance with Wulff's predictions) to see if that influence the emergence of plasticity during irradiation cascade [28–32]. Stacking fault tetrahedra (SFT), largely observed in these alloys are also considered. It is worth noticing that dislocation emission always begins from such pre-existing defects and that a clear influence of chromium is observed. It is interesting to note that in the vicinity of voids Shockley dislocations interact to form SFT defects and stair-rod ones [28].

II. COMPUTATIONAL METHODS

The atomistic behavior of the samples was modeled using the Molecular Dynamics method as implemented in the Large-scale Atomic Molecular Massively Parallel Simulator (LAMMPS) [33]. Interatomic potentials based on the embedded atom model (EAM) developed by Bonny *et al* [34, 35] were employed to describe atom-to-atom interactions. For computations, we initiated a numerical cell for pure Ni with [001] crystal orientations using the AtomsK numerical tool [36], employing a lattice constant of 0.352 nm. This initial configuration was then duplicated to create a supercell with varying volumes for different calculations in this study. Subsequently, alloy configurations were generated by introducing random substitutions in the supercell. This involved introducing 50% and 20% Fe for NiFe and NiFe₂₀ CSAs, 20% Cr for NiCr₂₀, and 40% Fe with 20% Cr for NiFeCr₂₀ CSAs. To account for randomness, computations were conducted across several different random alloy configurations.

The cells were relaxed using FIRE minimization algorithm until the force reaches 1×10^{-3} meV/Å [37] where the samples find their lowest energy structure. It is noteworthy that the optimization process for the CSAs' geometry was aimed at reaching the nearest local minimum of the energy structure ensuring that the change in energy between successive iterations and the most recent energy magnitude remains below 10^{-5} . Additionally, the global force vector length of all atoms is maintained at less than or equal to 10^{-8} eV/Å.

A. Molecular Static simulations

Point defects like vacancies where a missing atom at a lattice point can impact a CSAs' chemical properties and mechanical behavior during collision cascades are analyzed by computing the formation energy (E_v) of a vacancy, crucially determining the energy needed to break bonds and remove an atom from the crystal. To achieve this, we employ a computational cell containing $N_v =$

4000 atoms, with a lateral dimension of 3.52 nm. The vacancy energy is then calculated using the following method:

$$E_v = E_v^f - \frac{N_v - 1}{N_v} E_v^i, \quad (1)$$

where E_v^f and E_v^i are the total energy with the vacancy and the pristine one, respectively.

Then we checked 2D defects, surface and stacking fault. Surface energy of the (hkl) directions were computed following:

$$\Gamma_{hkl} = \frac{E_{\text{surf}} - E_0}{2S} \quad (2)$$

with E_{surf} the energy of the cell, E_0 the energy of the pristine cell and S the surface area.

10 different samples following the same atomic percentages for the CSAs were employed to ensure a reliable average of the Generalized Stacking Fault (GSF) energy, denoted as γ_{GSF} . The stacking fault was introduced by rigidly shifting the half upper region of the cell in the X and Y directions.

The energy of the cell, denoted as E_{GSF} , was then computed based on the displacement of the cell in the Y direction.

$$\gamma_{\text{GSF}} = \frac{E_{\text{GSF}} - E_0}{A} \quad (3)$$

with E_0 the energy of the pristine cell without the stacking fault and A is the GSF area.

In the third part we studied 3D defects. It is well-established that there are various defects in fcc metals [38]. Particularly, vacancy clusters and stacking fault tetrahedra (SFT) are prominently observed defects in these materials [39]. In this work, we decided to evaluate the impact of such defects (voids and SFT) on the irradiation cascade evolution. The procedure to introduce the defects is described in the following subsections.

Vacancy clusters were built by removing atoms within the geometric region defining the defect. We built voids of spherical, octahedral, and truncated octahedral shapes (as predicted by the Wulff theory using surface energies presented in the results section), as well as tetrahedral and cubic shapes. The Wulff theory, which relies on surface energy calculations across primary surface planes enables us to anticipate the stable configuration of vacancy clusters. This theory is in good agreement with atomistic simulations for sufficiently large clusters, where the faces of the cluster can be regarded as free surfaces. However, the theory encounters limitations when dealing with small clusters where the ratio of edge to face is high. Therefore, we initially investigated the stability of defects prior to irradiation cascade by employing Wulff theory alongside the analysis of formation energy results by using a Python package for Wulff construction [40, 41] to determine the Wulff shape using Γ_{100} , Γ_{110} and Γ_{111} .

The SFT was implemented employing the approach delineated in Ref. [42]. Following the same methodology

as for voids, we built a triangular vacancy plate that relaxed into SFT defects with stair-rod dislocations, due to the low stacking fault energy of the CSAs, as predicted by the Hirsch and Silcox mechanism [43].

To assess the stability of these defects prior to irradiation we computed the mean formation energy of each defects. For these peculiar simulations, the cells involved $N_{at} \simeq 863000$ atoms, arranged within dimensions $(d_x, d_y, d_z) = (21, 21, 21)$ nm. The defects were introduced as described before, and the mean formation energy per vacancy, E_f , of these defects was computed as follows:

$$E_f = \frac{1}{N_{at} - N_d} \left(E_d - \frac{N_d}{N_{at}} E_0 \right) \quad (4)$$

where E_d is the energy of the simulation cell with the defect, containing N_d atoms and $N_{at} - N_d$ vacancy and E_0 is the energy of the simulation cell of the pristine CSA, containing N_{at} atoms. We chose to rationalize the formation energy based on the number of vacancies, as defects of the same size can have different numbers of vacancies due to their unique shapes.

B. Collision cascades

The simulation cell size for a single collision cascade is selected to include all atoms within a radius r_0 (~ 3 Å), as discussed in [44, 45]. However, this size is insufficient for the trajectory of an implanted ion in the keV range. To address this, a larger cell ensures the recoiling atom is always surrounded by lattice atoms [46–48]. A pure fcc Ni sample with $(d_x, d_y, d_z) = (9.85, 10.20, 10.56)$ nm is initially created. After energy minimization, a 100 ps equilibration is conducted at 300 K with a time constant of 100 fs [49, 50].

As illustrated in Fig. 1, we considered two kind of defects: nanovoids and SFT, commonly found in this fcc metals [38]. The size of the defects is set to 2.0 nm. Regarding nanovoids, we analyzed the impact of their shape and performed tests on different geometries, encompassing spherical, octahedral, tetrahedral, and cubic shape.

MD simulations for collision cascades start with randomly selecting a Fe, Ni, or Cr atom at the center of the numerical sample. The Primary Knock-On Atom (PKA) receives kinetic energy (1–10 keV), and 50 simulations are conducted with arbitrary velocity direction. The Velocity Verlet integration algorithm models the cascade for 6 ps, followed by 4 ps relaxation, as shown in Fig. 1. A Nosé-Hoover thermostat cools the cell back to the initial temperature, simulating the bulk material's behavior. Pressure control is not applied during cascade simulations [26, 50, 51].

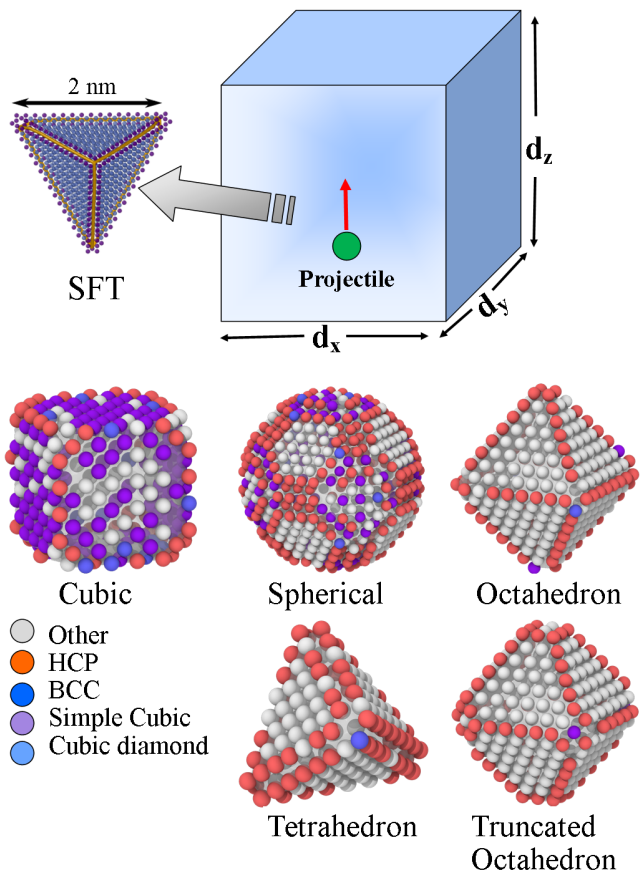


FIG. 1. (Color online) Schematics of the numerical cell utilized for conducting collision cascades, encompassing various defects such as cubic, spherical, octahedron, tetrahedron, truncated octahedron, and stacking fault tetrahedra. Initiated by assigning kinetic energy to a randomly selected atom-projectile, defects are characterized by identifying their atomic structure for enhanced visualization.

C. Analysis of collision cascades

The analysis of the formation of defects and dislocations during collision cascades is performed by computing the dislocation length as a function of simulation time for all the samples using OVITO software [52]. We utilized the polyhedral template matching (PTM) to identify different atomic structures and the Dislocation Extraction Algorithm (DXA) [53] which extracts dislocation structure and content from atomistic microstructures. Thus, we categorized the atomic structures as: BCC, FCC, HCP, icosahedral, simple cubic, and cubic diamond; the dislocations into several dislocation types according to their Burgers vectors as: $\frac{1}{2}\langle 110 \rangle$ (Perfect), $\frac{1}{6}\langle 112 \rangle$ (Shockley), $\frac{1}{6}\langle 110 \rangle$ (Stair-rod), $\frac{1}{3}\langle 100 \rangle$ (Hirth), $\frac{1}{3}\langle 111 \rangle$ (Frank). Then the dislocation density is obtained as

$$\rho(t) = L(t)/V_c \quad (5)$$

where $L(t)$ is the dislocation length of different types and V_c is the cell volume. In addition, the vacancies and voids are identified by the Delaunay tessellation to partition space into tetrahedral elements that are categorized as either solid or empty through the computation of an alpha parameter implemented into the surface mesh tool in OVITO [54].

III. RESULTS

It is noteworthy that Cr and Fe have the capability to modify the Stacking Fault Energy (SFE), a critical parameter in understanding dislocation behavior and the recovery process [55–58]. Materials with low SFE promote the formation of deformation twins, partial dislocations with a wide stacking fault ribbon, and a high stacking fault density [59, 60]. This stacking fault acts as a barrier against cross-slip or climb mechanisms, leading to slower recovery and the development of materials with high strength and good ductility. In contrast, materials with high SFE exhibit more rapid cross-slip and climb, resulting in a higher recovery rate [17, 61]. The modeling of radiation defects production has to accounting for the transfer of kinetic energy from high-energy incident particles to the lattice atoms in the surface sample.

Vacancy formation energies were calculated in good agreement with reported data by S. Zhao et al. [4], with values of 1.48 eV for pure Ni, $1.50 \text{ eV} \pm 0.2 \text{ eV}$ for NiFe₂₀ CSA while removing a Fe or a Ni atom; $1.70 \pm 0.2 \text{ eV}$ for equiatomic binary NiFe CSA; and $0.97 \pm 0.2 \text{ eV}$ for NiCr₂₀ CSA. Finally, our calculation for NiFeCr₂₀ CSA is $1.89 \pm 0.25 \text{ eV}$ in good agreement with reported data by Manzoor et al. [62]

A. Surface and Generalized Stacking Fault energy (GSF)

In order to provide information about the predefined defects in the alloys, we compute the surface energy of the pristine CSAs by using Eq. 1 that are displayed in Tab. I. Fe significantly increases the surface energy across all three surfaces, whereas the impact of chromium is comparatively less noticeable. However, neither Fe nor Cr altered the stability hierarchy among the three primary planes.

TABLE I. Surface energy Γ_{hkl} of the Ni, NiFe and NiFeCr systems computed using Eq. 2 in ($\text{meV}/\text{\AA}^2$)

	Γ_{100}	Γ_{110}	Γ_{111}
Ni	48.4	64.5	43.0
NiFe ₂₀	70 ± 2	85 ± 2	65 ± 2
NiFe	93 ± 2	106 ± 2	89 ± 2
NiCr ₂₀	58 ± 2	74 ± 2	53 ± 2
NiFeCr ₂₀	95 ± 2	74 ± 2	53 ± 2

Results for the GSF energies of the pristine CSAs are shown in Fig. 2 for all the systems. The intrinsic stacking fault energy is the metastable point of the GSF energy (see magnification on Fig. 2). We show a consistent decrease in the intrinsic stacking energy (see magnification in Fig. 2) with increasing the concentration of Fe or Cr solutes. This reduction is particularly prominent with Cr solutes, showcasing a substantial drop from $116 \text{ mJ}/\text{m}^2$ for pure Ni to $38 \text{ mJ}/\text{m}^2$ when Ni incorporates only 20% Cr. Conversely, the impact of Fe solutes is more subdued at $104 \text{ mJ}/\text{m}^2$ and escalates with an increasing number of Fe solutes, reaching $60 \text{ mJ}/\text{m}^2$ for NiFe alloys.

Intriguingly, both Fe and Cr solutes independently contribute to a decrease in intrinsic SFE. However, in the ternary alloy NiFeCr₂₀, the introduction of Fe solutes induces a noteworthy increase, up to $47 \text{ mJ}/\text{m}^2$, in intrinsic SFE compared to NiCr₂₀ alloys. Finally, to assess validity of the potential, our results were compared to those provided in Ref. [55, 63], for which more precise atomistic simulations were performed, employing Density Functional Theory method (DFT) (Fig. 2) reaching a good agreement.

B. Stability of defects before irradiation cascade

The predicted shape are depicted Fig. 3. Truncated octahedron are generally the preferred shape for vacancy clusters across all alloys, albeit with slight variations in the proportion of $\{110\}$ planes.

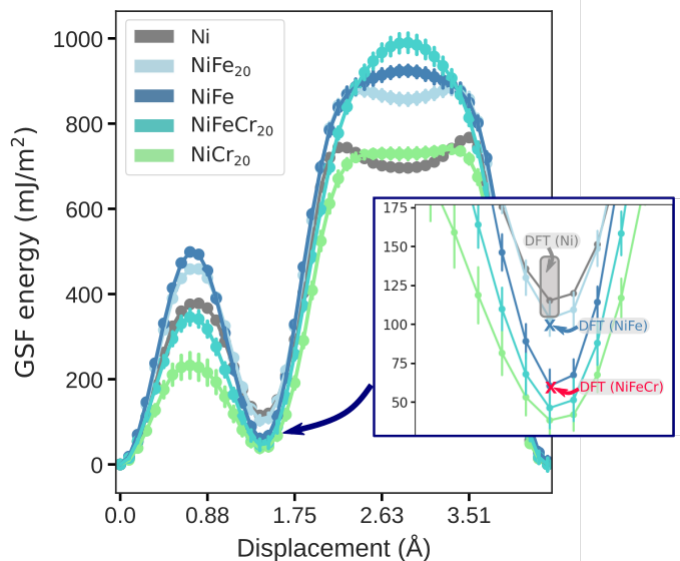


FIG. 2. Generalize the Stacking Fault energy across diverse alloy compositions compared to DFT [55, 63]. Uncertainties arise from the random distribution of solute atoms.

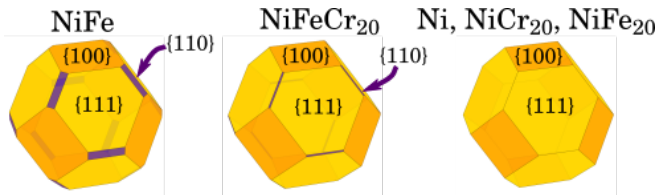


FIG. 3. Wulff shape predictions computed based on the surface energy of alloys (Table I)

1. Formation energy of defects

The results are shown Fig. 4, for all alloys and all defects. The results are averages derived from 10 different atomic configurations of alloys, and the associated error

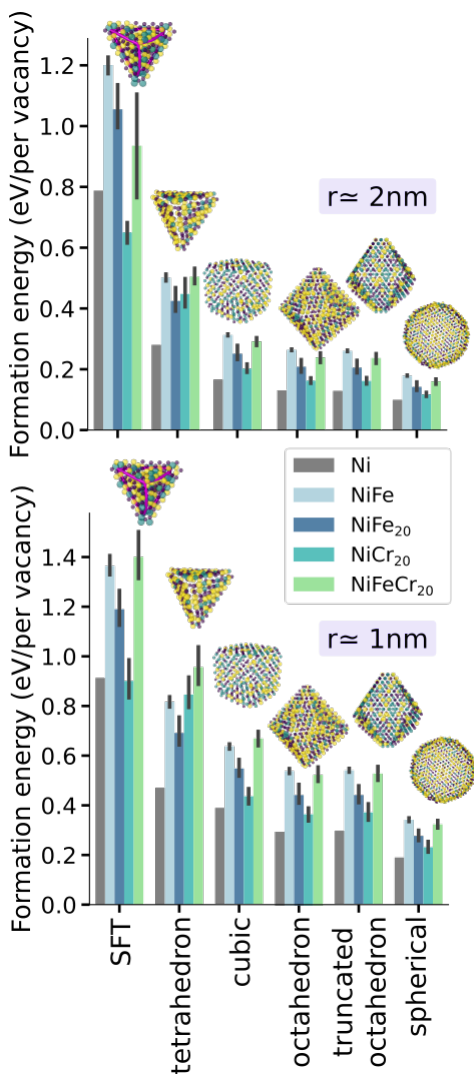


FIG. 4. Mean formation energy per vacancy of defects according to their shape and their size (r) for the different alloys. The results are averages derived from 10 different atomic configurations of alloys, and the associated error bars represent the standard deviations.

bars represent the standard deviations. When comparing the alloys, an observation is that the presence of Fe atoms leads to an increase in the defect formation energy. The highest formation energies are obtained in CSAs with the highest concentration of Fe, such as NiFe alloys, while the lowest formation energy is observed in binary NiCr CSAs. A lower formation energy indicates that defects form easily. Consequently, our findings suggest that the presence of iron may hinder the formation of vacancy clusters compared to both pure Ni and NiCr₂₀. According to our simulations spherical shape is the most stable, following by truncated octahedron and octahedron shape. The most unstable shape is tetrahedron cubic. SFT exhibit the highest formation energy; however, a direct comparison with voids is challenging because SFTs are composed of dislocation stair rods, not solely vacancies.

C. Collision cascade

Fig. 5 presents the outcomes of collision cascades involving pristine Ni and its CSAs for a defect-free sample in a), a cubic defect in b), and an spherical void in c). The temporal evolution of defects considered as atoms with a different structure than FCC during collision cascades is characterized by the phases of supersonic, sonic, and thermal recovery with respect to pure Ni, in good agreement with reported results [64]. Additionally, a notable effect observed in the solid solution alloys, compared to Ni, is the duration of the supersonic and sonic phases leading to the recovery phase. The influence of Fe and/or Cr atoms in the Ni sample is evident in the rapid production of defects by equiatomic NiFe and NiFeCr₂₀ alloys, where the inclusion of cubic and spherical defects modified the behaviour of the material changing the recovery time after collision cascade. The introduction of Cr in the Ni sample accelerates defect production after 0.1 ps, attributed to Ni-Cr and Cr-Cr interactions and the large decrease of the intrinsic stacking fault energy (Fig. 2), noticing a high defect production for the spherical void case. In the presence of Fe in NiFe_{50,20} and NiFeCr₂₀ CSAs, the material requires more time to recover. Conversely, the presence of Cr does not significantly impact these phases. These results are used as reference for our work.

To explore the impact of preexisting defects on point defect formation during collision cascades, MD simulations were conducted across various PKA values and materials. In Fig 5, we present results at 8 keV PKA, showcasing defect count profiles over simulation time for the most unstable defect vacancy (cubic) in b) and the most stable defect vacancy (spherical) in c), which can be considered as a void in the CSAs [65]; however, these defects can respond variably to irradiation. A comparison with the pristine case reveals observable changes in the defect production mechanism across all MD simulations. Additional results are available in the supplementary material. Distinct effects of Cr on defect production in Ni and

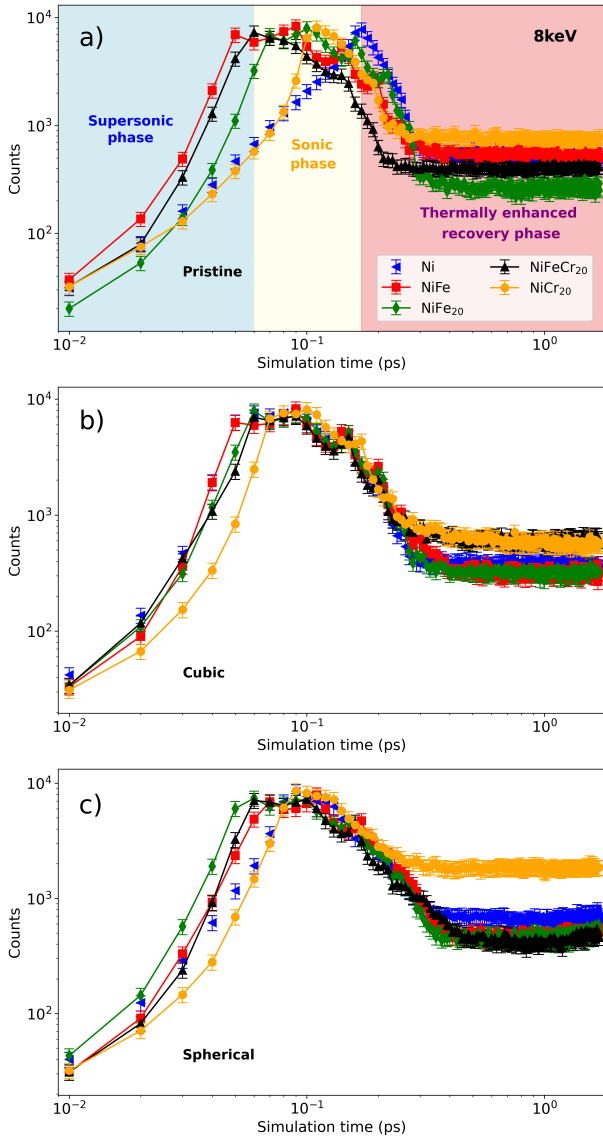


FIG. 5. (Color online) Typical time profiles depicting the number of defects during 8 keV cascades in Ni and its solid solution alloys for a defect-free sample in a), a cubic defect in b), and an spherical void in c). The three cascade stages—supersonic, sonic, and thermally enhanced recovery—are illustrated by the background colors in (a).

NiFe alloys were noted, leading to an increase in defect counts. Conversely, a small percentage of Fe in the Ni matrix resulted in reduced defect counts after the collision cascade in the pristine case. Intriguingly, when 50% of Fe is present in Ni, a drastic reduction in defects is observed for both cubic and SFT cases. This could potentially be an artifact of the Bonny potential [66].

In Fig. 6, the defects that are atoms with a different structure than FCC following collision cascades in all materials are illustrated in a heatmap graph within the PKA energy range of 1 to 10 keV. Panel a) represents the pristine case, b) displays a cubic vacancy, and c) showcases a

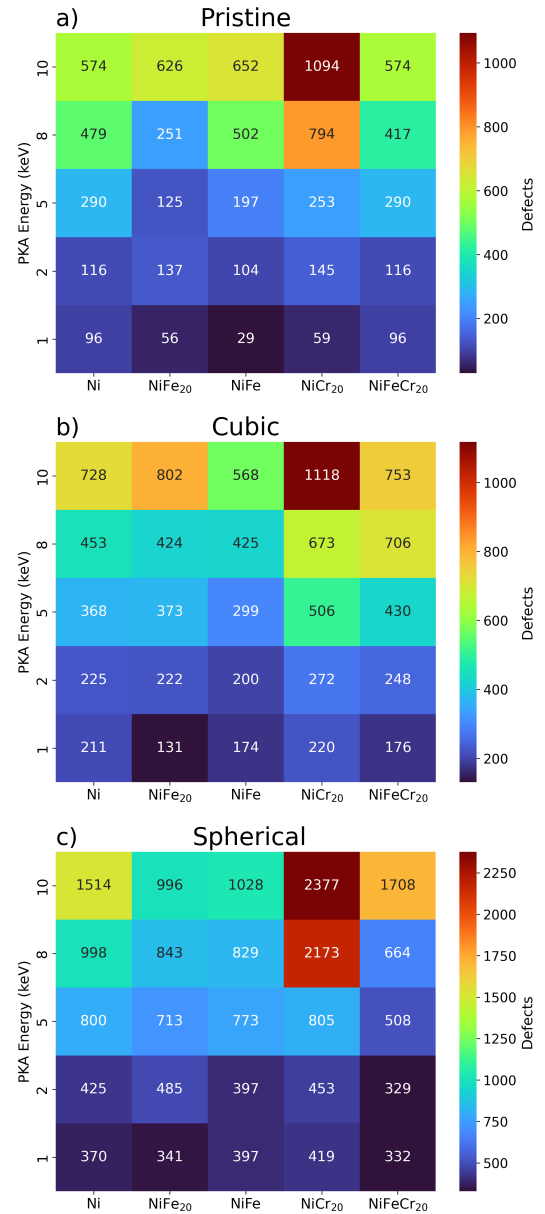


FIG. 6. (Color online). Heat mapping displays the total number of defects after collision cascades for the pristine material in (b); noticing the effect of Cr in the Ni matrix and NiFe alloys.

spherical void. It is evident that the presence of Fe atoms in the nickel sample reduces defect production compared to pure Ni, attributed to the soft bonding between Fe–Fe throughout the PKA range in the pristine and cubic vacancy scenarios. These results agree well with the results of the preliminary study, where we found that the formation energy of defects increases with Fe concentration, Fig. 4. However, defect production increases for the spherical void due to the surface energy associated with this defect. The reduction in defect production has been a subject of debate and may be attributed to

the potential [66]. However, the studies by Ullah et al. demonstrate that electron-phonon coupling induces defect recovery and strain relaxation in NiFe alloys [58]. Conversely, the presence of Cr in the Ni sample increases defect production due to Ni–Cr interactions, specially at high impact energies above 5 keV; regardless the shape of the preexisting defect or void. Of particular interest is the behavior of the NiFeCr₂₀ alloy after collision cascades, where the total defect production is comparable to pure Ni. This can be attributed to a compensation arising from the increase attributed to Cr solutes and the decrease due to Fe solutes.

In Fig. 7a), results depicting dislocation density as

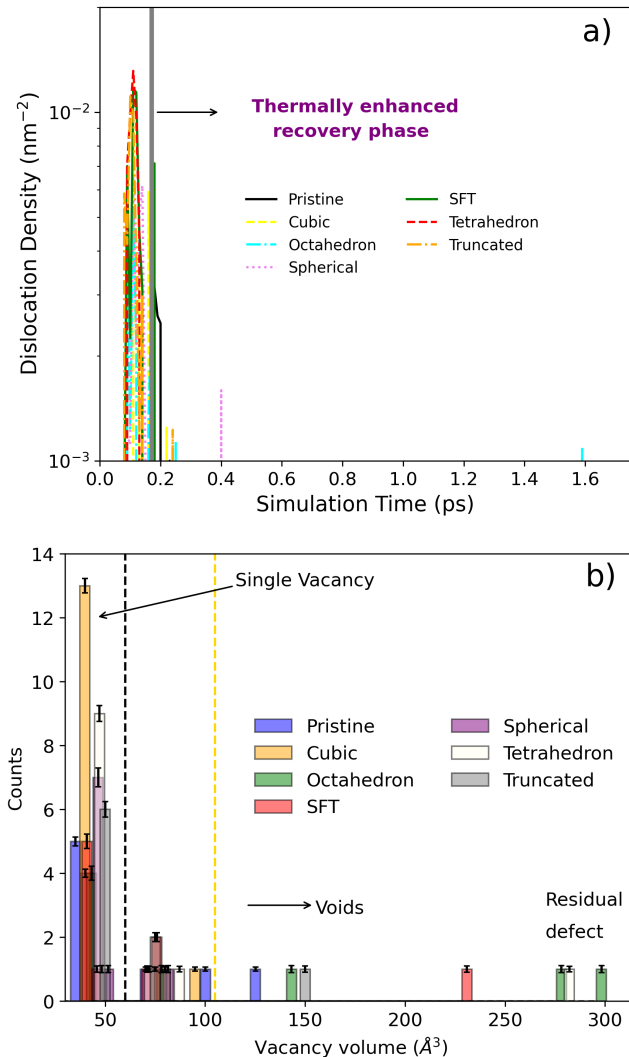


FIG. 7. (Color online) Dislocation density evolution in NiCr₂₀ depicted over simulation time for total dislocations in (a), Shockley partials in (b), and stair-rod dislocations in (c) at a PKA energy of 8 keV. It is noteworthy that the nucleation of stair-rod junction dislocations and their stabilities are predominantly influenced by the presence of Shockley partials across various vacancy defects.

a function of simulation time for a pure nickel sample with various preexisting defects at 8 keV of PKA are presented. In Fig. 7b), the quantification of single vacancies and the clustering of vacancies to form voids is displayed for different vacancy volumes. We observed that total dislocation nucleation occurs around the heat spike and diminishes during the material’s recovery, regardless of the defects present in the samples before cascades. However, the shape of the preexisting defect is crucial for the formation of vacancies and voids. In a pristine case, only single with a volume of $\sim 35 \text{ \AA}^3$ and di/tri vacancies are created. An unstable cubic defect can produce more single defects, and the most stable defect spherical void can only create single and di-vacancies. Finally, both a tetrahedron and its truncated form demonstrate the ability to generate substantial voids following collision cascades. The former yields residual defects characterized by a significant volume, akin to those produced by the octahedron defect.

D. The influence of Cr on dislocation nucleation.

To analyze the effects of the presence of Fe and Cr in the Ni matrices, Fig. 8 illustrates the results for the dislocation density over time in NiFe₂₀ in a), NiFe in b), NiCr₂₀ in c), and NiFeCr₂₀ in d), considering a cubic defect for total, Shockley partial, and Stair-rod dislocations. When 20% of Fe is in the Ni matrix, Shockley-type dislocations are nucleated around the heat spike in a similar way to the observed mechanisms for pure Ni. When the Fe concentration is increased to 50%, the Fe-Ni interaction and lattice mismatch make the Shockley partial dislocations more stable during the material’s recovery. The presence of Cr in the Ni matrix is observed to impact the material’s recovery, this is primarily due to lattice mismatch and interactions between Ni-Cr, Cr-Fe, and Cr-Cr in the sample.

During the heat spike of the collision cascade, the nucleation of partial Shockley dislocations is observed for all samples. Indeed, as the solutes induce a significant decrease in intrinsic stacking fault energy, they encourage the nucleation of Shockley partials and a high density of stacking fault. The interactions between different Shockley dislocations, as observed for the NiCr₂₀ and NiFeCr₂₀ alloys, can lead to the nucleation of Stair-rod dislocations in some cases, as outlined below:

$$\frac{1}{6}[110] = \frac{1}{6}[\bar{1}21] + \frac{1}{6}[2\bar{1}\bar{1}] \quad \text{Stair-rod}, \quad (6)$$

and other symmetrical cases. This is illustrated in Fig. 8c-d), where the Stair-rod dislocation stabilizes, and Shockley partials are annihilated after collision cascades a phenomenon further analyzed in subsequent sections of this manuscript.

An interesting effect is observed when adding 20% of Cr to the pure Ni and NiFe alloy, where the interaction between Ni,Fe and Cr stabilizes the nucleation of SFT

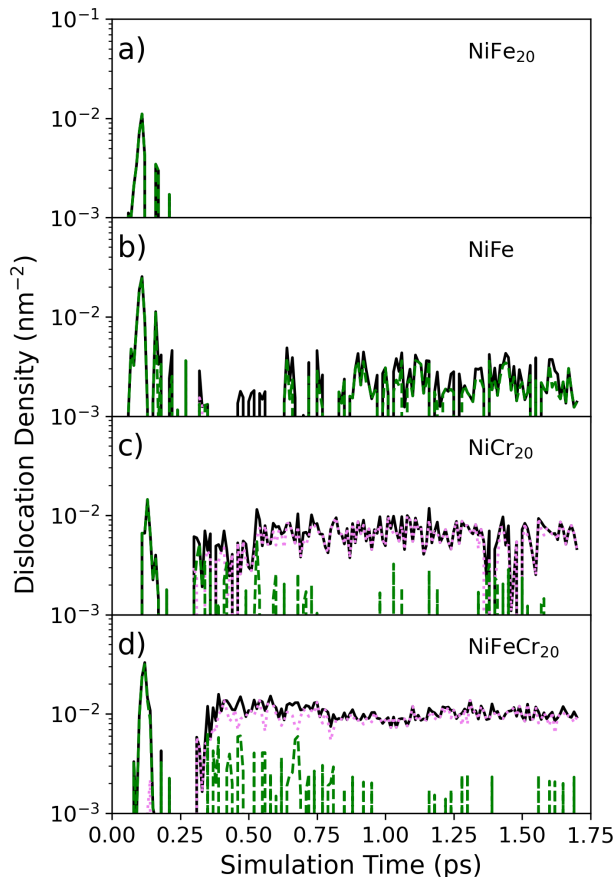


FIG. 8. (Color online). Dislocation density as a function of simulation time for (a) pure NiFe₂₀, (b) NiFe, (c) NiCr₂₀, and (d) NiFeCr₂₀ alloys, considering a cubic defect with an 8 keV Primary Knock-On Atom (PKA). The presence of Cr in either pure Ni and NiFe alloys promotes the nucleation of Stair-Rod dislocation. [64].

with a stair-rod dislocation during material recovery, as depicted in Fig. 9a-d). The presence of Fe and Cr atoms in the Ni matrix stabilizes the Shockley partials for certain defect vacancies, and the mechanism of the interaction of Shockley partials that nucleate a stair-rod junction persists. It is noteworthy that the nucleation of Shockley partials occurs during the material's recovery, where Ni and Fe exhibit similar lattice constants, while Cr has a smaller lattice constant. This lattice mismatch is further accentuated for the NiFeCr₂₀ alloy, where the conversion of one defect into another geometry is more prominently observed. For instance, in the case of spherical vacancy defects, they are transformed into three SFTs simultaneously.

In Fig. 10, we present the dislocation density over simulation time for NiFe₂₀ in (a), NiFe in (b), NiCr₂₀ in (c), and NiFeCr₂₀ in (d), considering a spherical void with 8 keV PKA. Noticing that the formation of stacking fault tetrahedra (SFT) is more pronounced in spherical defects within Cr-rich alloys. The chemical effects and

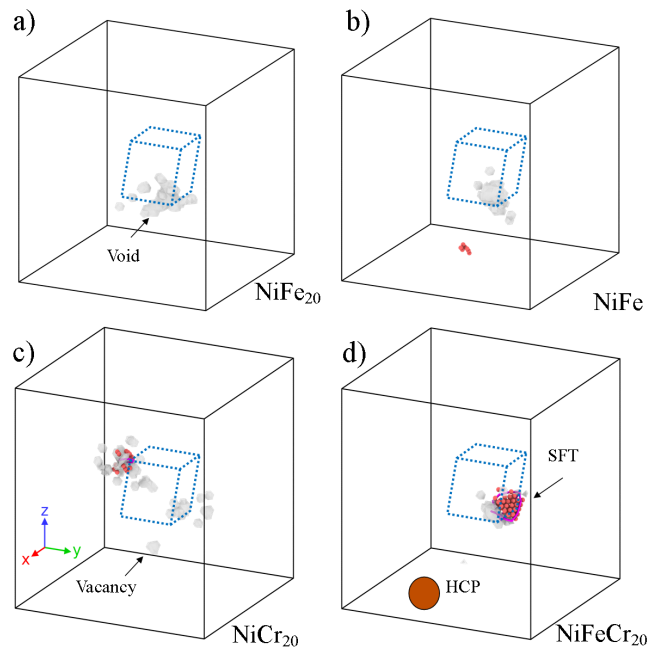


FIG. 9. (Color online) Visualizations of vacancies, void formation, and stacking fault tetrahedra (SFTs) identified by hexagonal close-packed (HCP) atoms after collision cascades. In pure NiFe alloys in a) and b), the distortion of the cubic defect is observed after collision cascades. In NiCr₂₀ alloy in c), the influence of Cr atoms promotes stair-rod dislocation formation and leads to SFT defects during material recovery. Similar effects are noted in NiFeCr₂₀ in d), where the interaction between Fe and Cr stabilizes the nucleation of SFT with stair-rod dislocation.

the decrease of the intrinsic stacking fault energy on the NiFe CSAs are again observed through the nucleation of stair-rod and Shockley dislocations during the material recovery phase. Specifically, the NiCr₂₀ alloy nucleates a couple of SFTs after collision cascades that is the alloy with the lowest stacking fault energy, while the NiFeCr₂₀ alloy forms three SFTs where the spherical defect was initially located. It is noteworthy that single collision cascades can transform unstable defects into stable ones, influencing plastic deformation mechanisms during irradiation experiments. Importantly, the formation of SFT is exclusively observed for these cubic and spherical defects among all considered defect types.

In Fig. 11 shows the visualizations of spherical voids, vacancies, and stacking fault tetrahedra (SFTs) identified by hexagonal close-packed (HCP) atoms post-collision cascades. For NiFe CSAs, the formation of voids, vacancies, and some self-interstitial atoms (SIAs) is distributed throughout the sample deforming the defect without formation of SFTs. In NiCr₂₀, the presence of Cr atoms has a significant impact on material recovery. Lattice mismatch and interactions between Cr-Cr and Cr-Ni promote the generation of stair-rod dislocations, ultimately leading to the creation of coupled SFTs defect post-collision cascades.

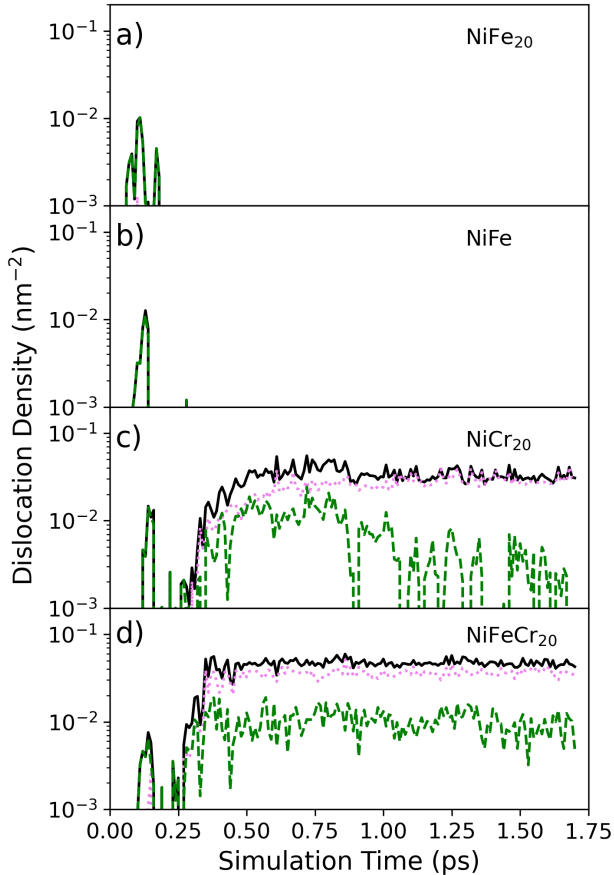


FIG. 10. (Color online). Dislocation density profiles over time for the spherical defect case at 8 keV PKA, illustrating the influence of chemistry on pure Ni (a), NiCr₂₀ (b), and NiFeCr₂₀ (c).

In Fig. 12 show the single vacancy and voids volume at the end of the collision cascade for cube defect in a) and a spherical void in b) at 8 keV. It is observed that NiFe CSAs for cubic are able to create sets of 3 vacancies, while Cr presence in Ni and NiFe CSAs tents to deform the cube defect into several single vacancies. For the spherical void, the NiFe CSAs deforms the void into sets of single and di vacancies, while Cr generates sets of single vacancies and a big void (roughly 6 vacancies) located at the center of the initial void. This effect is due to the GSF energy associated to the Cr-rich alloys as presented in Fig 1.

IV. CONCLUDING REMARKS

Summarizing, our computational exploration of single-phase concentrated solid-solution alloys (SP-CSAs) has provided valuable insights into the complex dynamics of irradiation-induced defects. By conducting molecular dynamics simulations across a spectrum of CSAs, ranging from pure Ni, passing through binary alloys NiFe_{20,50} and

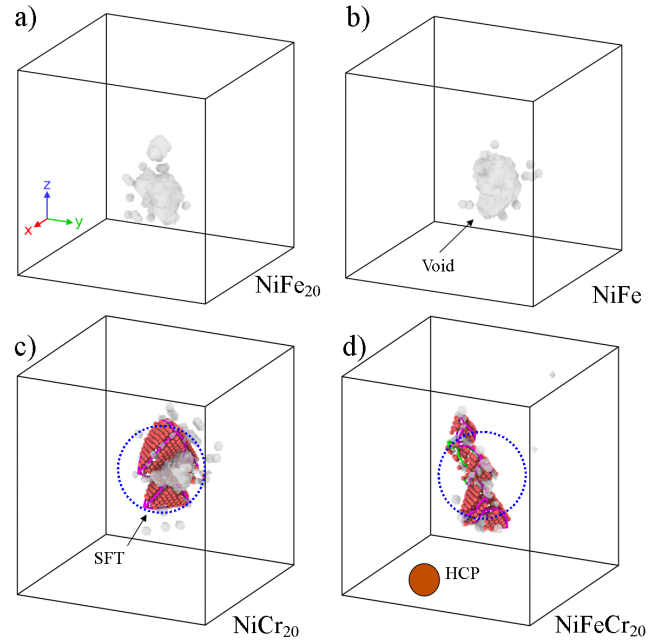


FIG. 11. (Color online) The recovery phase reveals nucleation of stair-rod and Shockley dislocations, with NiCr₂₀ alloy forming a couple of stacking fault tetrahedra (SFTs), and NiFeCr₂₀ alloy forming three SFTs at the location of the initial spherical defect. Notably, SFT formation is exclusively observed for cubic and spherical defects among all considered defect types.

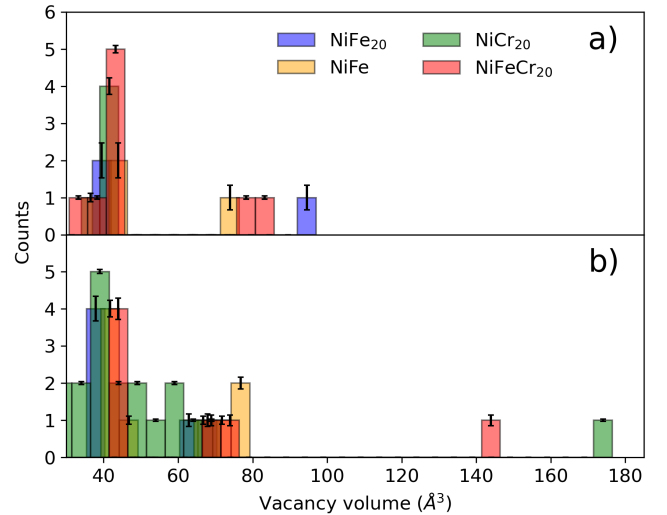


FIG. 12. (Color online) Variation in vacancy counts as a function of their volume for different materials. Panel (a) illustrates the scenario with a cube defect, while panel (b) represents a spherical void, both simulated at 8 keV. It is evident that the presence of Cr in the Ni and NiFe CSAs significantly influences both defects, leading to the production of a greater number of single vacancies.

NiCr₂₀, to Ni₄₀Fe₄₀Cr₂₀, and varying PKA energies, we unraveled the interplay between alloying elements and

defect evolution. The modeling framework, considering a diverse array of vacancy defects, illuminated a remarkable transition from spherical vacancy (voids) defects to stacking fault tetrahedra (SFTs). This transformation was intricately linked to the material's chemical composition, on the stacking fault energy of the alloys, by an analysis of the dislocation nucleation and evolution as a function of the dynamics time, with only Cr-rich alloys exhibiting the nucleation of stair-rod dislocations, ultimately leading to the formation of stable SFTs. Notably, NiCr₂₀ and NiFeCr₂₀ emerged as the exclusive materials capable of this intriguing mechanism. Indeed, both alloys exhibit very low stacking fault energies, facilitating the nucleation of SFTs validated by molecular static simulations to compute the surface, vacancy, and defect formation energies.

These findings underscore the pivotal role of alloy chemistry in dictating irradiation-induced defect dynamics. The observed mechanisms, including the conversion to SFTs, hold implications for the irradiation resistance of SP-CSAs. This study contributes to a understanding of the nanoscale phenomena governing vacancy defect evolution for informed material design strategies to

enhance irradiation tolerance.

ACKNOWLEDGEMENTS

Research was funded through the European Union Horizon 2020 research and innovation program under Grant Agreement No. 857470 and from the European Regional Development Fund under the program of the Foundation for Polish Science International Research Agenda PLUS, grant No. MAB PLUS/2018/8, and the initiative of the Ministry of Science and Higher Education 'Support for the activities of Centers of Excellence established in Poland under the Horizon 2020 program' under agreement No. MEiN/2023/DIR/3795. Computational resources were provided by the High Performance Cluster at the National Centre for Nuclear Research in Poland. We would like to express our gratitude to NOETHER computing facilities at La Rochelle University and MCIA (Mésocentre de Calcul Intensif Atlantique). Additionally, we extend our gratitude to GENCI - (CINES/CCRT), under Grant number A0110913037.

-
- [1] C. Lu, L. Niu, N. Chen, *et al.*, *Nature Communications* **7**, 13564 (2016).
- [2] M. W. Ullah, H. Xue, G. Velisa, *et al.*, *Scientific Reports* **7**, 4146 (2017).
- [3] B. D. Wirth, *Science* **318**, 923 (2007), <https://www.science.org/doi/pdf/10.1126/science.1150394>.
- [4] S. Zhao, G. M. Stocks, and Y. Zhang, *Phys. Chem. Chem. Phys.* **18**, 24043 (2016).
- [5] M. Kan, D. Brigitte, F. Anna, P. Frederic, and L.-P. Marie, *Materials Research Letters* **8**, 201 (2020).
- [6] M. Kan, D. Brigitte, F. Anna, J. Thomas, P. Frederic, and L.-P. Marie, *Acta Materialia* **212**, 116874 (2021).
- [7] M. W. Ullah, D. S. Aidhy, Y. Zhang, and W. J. Weber, *Acta Materialia* **109**, 17 (2016).
- [8] T. Egami, W. Guo, P. D. Rack, *et al.*, *Metallurgical and Materials Transactions A* **45**, 180 (2014).
- [9] G. Pintsuk, E. Diegele, S. L. Dudarev, M. Gorley, J. Henry, J. Reiser, and M. Rieth, *Fusion Engineering and Design* **146**, 1300 (2019), sI:SOFT-30.
- [10] F. Granberg, K. Nordlund, M. W. Ullah, K. Jin, C. Lu, H. Bei, L. M. Wang, F. Djurabekova, W. J. Weber, and Y. Zhang, *Phys. Rev. Lett.* **116**, 135504 (2016).
- [11] K. Jin, C. Lu, L. Wang, J. Qu, W. Weber, Y. Zhang, and H. Bei, *Scripta Materialia* **119**, 65 (2016).
- [12] L. Kurpaska, F. J. Dominguez-Gutierrez, Y. Zhang, K. Mulewska, H. Bei, W. J. Weber, A. Kosińska, W. Chrominski, I. Jozwik, R. Alvarez-Donado, *et al.*, *Materials & Design* **217**, 110639 (2022).
- [13] Y. Zhang, K. Jin, H. Xue, C. Lu, R. J. Olsen, L. K. Beland, M. W. Ullah, S. Zhao, H. Bei, D. S. Aidhy, *et al.*, *Journal of Materials Research* **31**, 2363 (2016).
- [14] K. Karimi, A. Esfandiarpour, R. Alvarez-Donado, M. J. Alava, and S. Papanikolaou, *Phys. Rev. B* **105**, 094117 (2022).
- [15] R. Alvarez-Donado, S. Papanikolaou, A. Esfandiarpour, and M. J. Alava, *Phys. Rev. Mater.* **7**, 025603 (2023).
- [16] O. Deluigi, R. Pasianot, F. Valencia, A. Caro, D. Farkas, and E. Bringa, *Acta Materialia* **213**, 116951 (2021).
- [17] Z. Wu, H. Bei, F. Otto, G. M. Pharr, and E. P. George, *Intermetallics* **46**, 131 (2014).
- [18] B. Gludovatz, A. Hohenwarter, D. Catoor, E. H. Chang, E. P. George, and R. O. Ritchie, *Science* **345**, 1153 (2014).
- [19] O. Senkov, G. Wilks, D. Miracle, C. Chuang, and P. Liaw, *Intermetallics* **18**, 1758 (2010).
- [20] T. Yang, C. Li, S. J. Zinkle, S. Zhao, H. Bei, and Y. Zhang, *Journal of Materials Research* **33**, 3077 (2018).
- [21] S. J. Zinkle and G. Was, *Acta Materialia* **61**, 735 (2013).
- [22] T. Allen, J. Busby, M. Meyer, and D. Petti, *Materials today* **13**, 14 (2010).
- [23] A. M. Goryaeva, C. Domain, A. Chartier, *et al.*, *Nature Communications* **14**, 3003 (2023).
- [24] A. Debelle, J.-P. Crocombette, A. Bouille, A. Chartier, T. Jourdan, S. Pellegrino, D. Bachiller-Perea, D. Carpentier, J. Channagiri, T.-H. Nguyen, F. Garrido, and L. Thomé, *Phys. Rev. Mater.* **2**, 013604 (2018).
- [25] K. Arakawa, M.-C. Marinica, S. Fitzgerald, L. Proville, D. Nguyen-Manh, S. L. Dudarev, P.-W. Ma, T. D. Swinburne, A. M. Goryaeva, T. Yamada, *et al.*, *Nature Materials* **19**, 508 (2020).
- [26] A. Chartier and M.-C. Marinica, *Acta Materialia* **180**, 141 (2019).
- [27] P. Chen, A. Chesetti, and M. J. Demkowicz, *Journal of Nuclear Materials* **555**, 153124 (2021).
- [28] M. L. Dos Reis, L. Proville, M.-C. Marinica, and M. Sauzay, *Physical Review Materials* **4**, 103603 (2020).
- [29] C. Boukouvala, J. Daniel, and E. Ringe, *Nano Convergence* **8**, 26 (2021).

- [30] B. P. Uberuaga, R. G. Hoagland, A. F. Voter, and S. M. Valone, *Phys. Rev. Lett.* **99**, 135501 (2007).
- [31] T. Niu, S. Rayaprolu, Z. Shang, T. Sun, C. Fan, Y. Zhang, C. Shen, M. Nasim, W. ying Chen, M. Li, Y. Xue, H. Wang, A. El-Azab, and X. Zhang, *Materials Today Communications* **33**, 104418 (2022).
- [32] Q. Liang, S. Weng, T. Fu, S. Hu, and X. Peng, *Materials Chemistry and Physics* **282**, 125997 (2022).
- [33] A. P. Thompson, H. M. Aktulga, R. Berger, D. S. Bolinteanu, W. M. Brown, P. S. Crozier, P. J. in 't Veld, A. Kohlmeyer, S. G. Moore, T. D. Nguyen, R. Shan, M. J. Stevens, J. Tranchida, C. Trott, and S. J. Plimpton, *Computer Physics Communications* **271**, 108171 (2022).
- [34] G. Bonny, A. BakaeV, P. Olsson, C. Domain, E. Zhurkin, and M. Posselt, *Journal of Nuclear Materials* **484**, 42 (2017).
- [35] G. Bonny, N. Castin, and D. Terentyev, *Modelling and Simulation in Materials Science and Engineering* **21**, 085004 (2013).
- [36] P. Hirel, *Computer Physics Communications* **197**, 212 (2015).
- [37] J. Guenol , W. G. N hring, A. Vaid, F. Houll , Z. Xie, A. Prakash, and E. Bitzek, *Computational Materials Science* **175**, 109584 (2020).
- [38] B. Eyre, *J. Phys. F: Met. Phys.* **3**, 422 (1973).
- [39] D. Chakraborty and D. S. Aidhy, *Journal of Alloys and Compounds* **725**, 449 (2017).
- [40] L. Marks, *Journal of Crystal Growth* **61**, 556 (1983).
- [41] G. Wulff, *Z. Kristallogr* **34**, 449 (1901).
- [42] T. Kadoyoshi, H. Kaburaki, F. Shimizu, H. Kimizuka, S. Jitsukawa, and J. Li, *Acta Mater.* **55**, 3073 (2007).
- [43] J. Silcox and P. Hirsch, *Philos. Mag.* **4**, 72 (1959).
- [44] K. Nordlund, *Computational Materials Science* **3**, 448 (1995).
- [45] K. Nordlund, S. Zinkle, A. Sand, F. Granberg, R. Averback, R. Stoller, T. Suzudo, T. Malerba, F. Banhart, W. Weber, F. Willaime, S. Dudarev, and D. Simeone, *Nature Communications* **9**, 1084 (2018).
- [46] K. Nordlund, S. J. Zinkle, A. E. Sand, *et al.*, *Nature Communications* **9**, 1084 (2018).
- [47] A. Boule, A. Chartier, A. Debelle, X. Jin, and J.-P. Combette, *Journal of Applied Crystallography* **55**, 296 (2022).
- [48] K. Nordlund, S. J. Zinkle, A. E. Sand, F. Granberg, R. S. Averback, R. E. Stoller, T. Suzudo, L. Malerba, F. Banhart, W. J. Weber, F. Willaime, S. L. Dudarev, and D. Simeone, *Journal of Nuclear Materials* **512**, 450 (2018).
- [49] F. J. Dominguez-Gutierrez, A. Ustrzycka, Q. Q. Xu, R. Alvarez-Donado, S. Papanikolaou, and M. J. Alava, *Modelling and Simulation in Materials Science and Engineering* **30** (2022).
- [50] F. J. Dom nguez-Guti rrez, J. Byggm rstar, K. Nordlund, F. Djurabekova, and U. von Toussaint, *Modelling and Simulation in Materials Science and Engineering* **29**, 055001 (2021).
- [51] M. Koskenniemi, J. Byggm rstar, K. Nordlund, and F. Djurabekova, *Journal of Nuclear Materials* **577**, 154325 (2023).
- [52] A. Stukowski, *Modelling and simulation in materials science and engineering* **18**, 10.1088/0965-0393/18/1/015012 (2010).
- [53] A. Stukowski, *Modelling and Simulation in Materials Science and Engineering* **18**, 015012 (2009).
- [54] A. Stukowski, *JOM* **66**, 399 (2014).
- [55] A. Zaddach, C. Niu, C. Koch, and D. Irving, *Jom* **65**, 1780 (2013).
- [56] R. E. Schramm and R. P. Reed, *Metallurgical Transactions A* **7**, 359 (1976).
- [57] C. Carter and S. Holmes, *The Philosophical Magazine: A Journal of Theoretical Experimental and Applied Physics* **35**, 1161 (1977).
- [58] M. W. Ullah, N. Sellami, A. Leino, H. Bei, Y. Zhang, and W. J. Weber, *Computational Materials Science* **173**, 109394 (2020).
- [59] K. Youssef, M. Sakaliyska, H. Bahmanpour, R. Scattergood, and C. Koch, *Acta Materialia* **59**, 5758 (2011).
- [60] X. Wu, X. San, X. Liang, Y. Gong, and X. Zhu, *Materials & Design* **47**, 372 (2013).
- [61] Y. Gong, C. Wen, Y. Li, X. Wu, L. Cheng, X. Han, and X. Zhu, *Materials Science and Engineering: A* **569**, 144 (2013).
- [62] A. Manzoor, G. Arora, B. Jerome, N. Linton, B. Norman, and D. S. Aidhy, *Frontiers in Materials* **8**, 10.3389/fmats.2021.673574 (2021).
- [63] S. Zhao, G. M. Stocks, and Y. Zhang, *Acta Materialia* **134**, 334 (2017).
- [64] G. Fabris, N. Marana, E. Longo, and J. Sambrano, *Journal of Solid State Chemistry* **258**, 247 (2018).
- [65] M. Landeiro Dos Reis, L. Proville, M.-C. Marinica, and M. Sauzay, *Phys. Rev. Mater.* **4**, 103603 (2020).
- [66] L. K. B land, A. Tamm, S. Mu, G. D. Samolyuk, Y. N. Osetsky, A. Aabloo, M. Klintonberg, A. Caro, and R. E. Stoller, *Computer Physics Communications* **219**, 11 (2017).